The Propagation of Coherent Waves Across Multiple Solar Magnetic Pores

S. D. T. Grant[1], D. B. Jess[1,2], M. Stangalini[3], S. Jafarzadeh[4,5], V. Fedun[6], G. Verth[7], P. H. Keys[1],
S. P. Rajaguru[8], H. Uitenbroek[9], C. D. MacBride[1], W. Bate[1], and C. A. Gilchrist-Millar[1]

[1] Astrophysics Research Centre, School of Mathematics and Physics, Queen's University Belfast, Belfast, BT7 1NN, UK; samuel.grant@qub.ac.uk
[2] Department of Physics and Astronomy, California State University Northridge, Northridge, CA 91330, USA
[3] ASI, Italian Space Agency, Via del Politecnico snc, I-00133, Rome, Italy
[4] Leibniz Institute for Solar Physics (KIS), Schöneckstr. 6, D-79104 Freiburg, Germany
[5] Rosseland Centre for Solar Physics, University of Oslo, P.O. Box 1029 Blindern, NO-0315 Oslo, Norway
[6] Plasma Dynamics Group, Department of Automatic Control and Systems Engineering, The University of Sheffield, Mappin Street, Sheffield, S1 3JD, UK
[7] Plasma Dynamics Group, School of Mathematics and Statistics, The University of Sheffield, Hicks Building, Hounsfield Road, Sheffield, S3 7RH, UK
[8] Indian Institute of Astrophysics, Bangalore-34, India
[9] National Solar Observatory, University of Colorado Boulder, 3665 Discovery Drive, Boulder, CO, 80303, USA

Abstract

Solar pores are efficient magnetic conduits for propagating magnetohydrodynamic wave energy into the outer regions of the solar atmosphere. Pore observations often contain isolated and/or unconnected structures, preventing the statistical examination of wave activity as a function of the atmospheric height. Here, using high-resolution observations acquired by the Dunn Solar Telescope, we examine photospheric and chromospheric wave signatures from a unique collection of magnetic pores originating from the same decaying sunspot. Wavelet analysis of high-cadence photospheric imaging reveals the ubiquitous presence of slow sausage-mode oscillations, coherent across all photospheric pores through comparisons of intensity and area fluctuations, producing statistically significant in-phase relationships. The universal nature of these waves allowed an investigation of whether the wave activity remained coherent as they propagate. Utilizing bisector Doppler velocity analysis of the Ca II 8542 Å line, alongside comparisons of the modeled spectral response function, we find fine-scale 5 mHz power amplification as the waves propagate into the chromosphere. Phase angles approaching zero degrees between co-spatial line depths spanning different line depths indicate standing sausage modes following reflection against the transition region boundary. Fourier analysis of chromospheric velocities between neighboring pores reveals the annihilation of the wave coherency observed in the photosphere, with examination of the intensity and velocity signals from individual pores indicating they behave as fractured waveguides, rather than monolithic structures. Importantly, this work highlights that wave morphology with atmospheric height is highly complex, with vast differences observed at chromospheric layers, despite equivalent wave modes being introduced into similar pores in the photosphere.

Unified Astronomy Thesaurus concepts: Solar chromosphere (1479); Magnetohydrodynamics (1964); Solar oscillations (1515); Solar photosphere (1518); Solar magnetic fields (1503)

1. Introduction

The mechanisms by which the upper solar atmosphere maintains its heightened temperature remain at the forefront of solar physics (Parnell & De Moortel 2012; Van Doorsselaere et al. 2020). The corona has long been the focus of this interest, due in part to the extraordinary temperatures observed, in excess of 1 MK, but also to the availability of a range of data products alongside models capable of replicating the physics of this optically thin region (Banerjee et al. 2007; De Moortel & Browning 2015). In contrast, the chromosphere is a challenging observational project, with less than 1% of observed solar emission emanating from this tenuous region (Jess et al. 2010b), and relatively few absorption lines sensitive to chromospheric activity (Vernazza et al. 1981). However, the chromosphere demands an order of magnitude greater energy flux than the corona to maintain a temperature of ∼10,000 K (Withbroe & Noyes 1977), placing a greater importance on identifying the heating processes at these lower heights.

In the denser and partially ionized chromosphere, large-scale current sheet formation and flare activity have not been shown to effectively heat localized plasma (Socas-Navarro 2005). Instead, the tentative observational evidence of nanoflares presents the only postulated mechanism for chromospheric flare heating (Jess et al. 2014; Priest et al. 2018; Jess et al. 2019). In contrast, there is an abundance of magnetohydrodynamic (MHD) wave observations (see the reviews of Jess et al. 2015; Verth & Jess 2016; Srivastava et al. 2021) to corroborate the previously proposed dissipation of waves generated at the solar surface into localized chromospheric plasma (e.g., Schwarzschild 1948; Leighton et al. 1962; Noyes & Leighton 1963). In subsequent studies of wave generation and propagation in the lower atmosphere, it became clear that, despite oscillations being generated across the entire solar surface, the majority of which are in the 3–5 minute *p*-mode periodicity range (Braun et al. 1988), much of this acoustic energy flux could not penetrate into the chromosphere, either through wave reflection at the chromospheric boundary, or shock formation at lower heights (Narain & Ulmschneider 1996; Fossum & Carlsson 2005a). Rather, the strong, vertical magnetic fields of active regions can guide global resonant MHD wave modes into the upper regions of the

atmosphere to influence heating (Bel & Leroy 1977; Khomenko & Collados 2015).

Magnetic pores are often considered as the pre-cursor, or aftermath to, the formation of a sunspot (Garcia De La Rosa 1987). Their smaller size and field strengths in comparison to sunspots make them more dynamic and reactive to wave generation mechanisms, such as convective buffeting (Sobotka 2003), while having lifetimes far exceeding other smaller magnetic flux tubes (Keys et al. 2014). As a result, there has been a plethora of modern observations of various MHD wave modes within pores (e.g., Centeno et al. 2009; Stangalini et al. 2011, 2012; Cho et al. 2015). In particular, compressible sausage-mode waves have been prevalent in the lower atmosphere as their first detection (Dorotovič et al. 2008), distinguished from other modes through complementary intensity and cross-sectional area oscillations in the pore (Edwin & Roberts 1983; Morton et al. 2011; Moreels et al. 2013). Sausage-mode signatures have confirmed the viability of pores as waveguides across the solar surface, where Keys et al. (2018) observed both surface and body modes to be ubiquitous within a large sample of photospheric pores. These compressible motions within pores have also been seen to propagate into the chromosphere, with extensive wave damping along their direction of propagation of approximately $50,000 \, \mathrm{W \, m^{-2}}$ between the photospheric and chromospheric layers (Grant et al. 2015; Moreels et al. 2015).

Recently, Gilchrist-Millar et al. (2021, henceforth referred to as GM21) employed inversions of spectropolarimetric Si I 10827 Å data to further constrain sausage-mode damping in a series of adjacent pores, with further identification of extensive wave damping in the range of $25,000-30,000 \, \mathrm{W \, m^{-2}}$ in the lower solar atmosphere. Subsequent modeling of this damping was conducted by Riedl et al. (2021), proposing that localized drivers in the pore were generating the sausage modes, which were damped as a result of wave leakage from the body of the pore, alongside geometric effects from the attenuation of the magnetic field as a function of the height. In this study, complementary imaging data to the products used by GM21 are used to infer the nature of the photospheric wave driver in order to confirm the proposed damping mechanisms of Riedl et al. (2021). Further, the nature of the observed waves as they bridge into the chromosphere is assessed alongside whether the properties of each pore have an effect on wave propagation, using chromospheric spectral data that are characterized further with future solar missions in mind.

2. Observations and Data Processing

The data presented here is an observational sequence obtained during 14:09–15:59 UT on 2016 July 12 with the Dunn Solar Telescope (DST) at Sacramento Peak, New Mexico. The telescope was focused on the active region NOAA 12564, positioned at heliocentric coordinates $(-425'', 98'')$, or N10.4E27.5 in the conventional heliographic coordinate system (see Figure 1).

The Interferometric BIdimensional Spectrometer (IBIS; Cavallini 2006) was utilized to sample the Ca II absorption profile at 8542.12 Å with 47 nonequidistant wavelength steps employed covering ± 1.3 Å from the line core (see Figure 2). The IBIS instrument imaged a $97'' \times 97''$ (approximately $70 \times 70 \, \mathrm{Mm^2}$) region of the solar disk, with a spatial sampling of $0''.098$ (71 km) per pixel and temporal cadence of 9.4 s per full scan (see Figure 3). A white-light camera, synchronized

with the narrowband channel, was also utilized to further correct for seeing effects in the narrowband images. The narrowband images were destretched using co-spatial and co-temporal vectors calculated from a dense grid of subfield kernels applied to the white-light image sequence (following the methodology applied in Jess et al. 2007, 2010a; Grant et al. 2018). Fourier analysis of the destretch vectors confirmed that such corrections did not add spurious oscillatory power at any frequency under consideration in this study. A blueshift correction was also applied to all narrowband images to account for the use of classical etalon mountings (Cauzzi et al. 2008).

The Rapid Oscillations in the Solar Atmosphere (ROSA; Jess et al. 2010b) camera system was used to image a $145'' \times 145''$ portion of the solar disk through a continuum (4170 Å) filter, at a spatial sampling of $0''.155$ per pixel (see Figure 1). The image clarity from both instruments were improved using techniques of high-order adaptive optics (Rimmele 2004) and Fourier co-alignment (Jess et al. 2007). For the ROSA imaging data, speckle reconstruction (Wöger et al. 2008) was also applied. Utilizing $64 \rightarrow 1$ speckle restorations, the resulting cadence for the continuum image sequence was 2.11 s.

The seeing remained good for the initial phase of observing, but deteriorated toward the end of the time series, in particular for the 4170 Å continuum ROSA images that were obtained in the near-UV portion of the electromagnetic spectrum. Given the importance of accurately tracking the two-dimensional pore boundaries, only the first 62 minutes of data are used in our study, equating to 400 IBIS scans and 1800 ROSA images.

3. Analysis and Discussion

Within the field of view, a set of magnetic pores are present, formed as a result of the decay and break up of a sunspot. The rate of magnetic field dispersion in this active region is significant, and thus smaller magnetic flux concentrations disappear over the observing period. Five larger magnetic pores are identified throughout the observing time in GM21, the properties of which are presented in Table 1, as a result of the Stokes inversion based on response functions (SIR; Ruiz Cobo & del Toro Iniesta 1992) analysis of the photospheric Si I 10827 Å line (except the area that is determined by intensity thresholding; see below). It is evident that these pores present in a unique configuration, worthy of study at higher spatial and temporal resolution using complementary data products. Initial importance is placed on the interaction of these pores in the low photosphere, and whether they act as individual flux tubes or retain the monolithic behavior of the preceding sunspot (e.g., consistent with the coherent umbral dynamics presented in Jess et al. 2012a; Yuan et al. 2014; Jess et al. 2016, 2017; Stangalini et al. 2021; Albidah et al. 2021).

3.1. Photospheric Interactions

The 4170 Å ROSA continuum filter, which images a height of ~ 25 km above the solar surface (Jess et al. 2012b), was utilized to assess the pores as they become visible in the solar atmosphere. Intensity thresholding was applied to isolate the pores in the image set, in a similar manner to Grant et al. (2015). A quiescent region, free of any extraneous magnetic brightenings (the green region outlined in Figure 1) was used to derive a characteristic mean intensity, I_{mean}, and standard
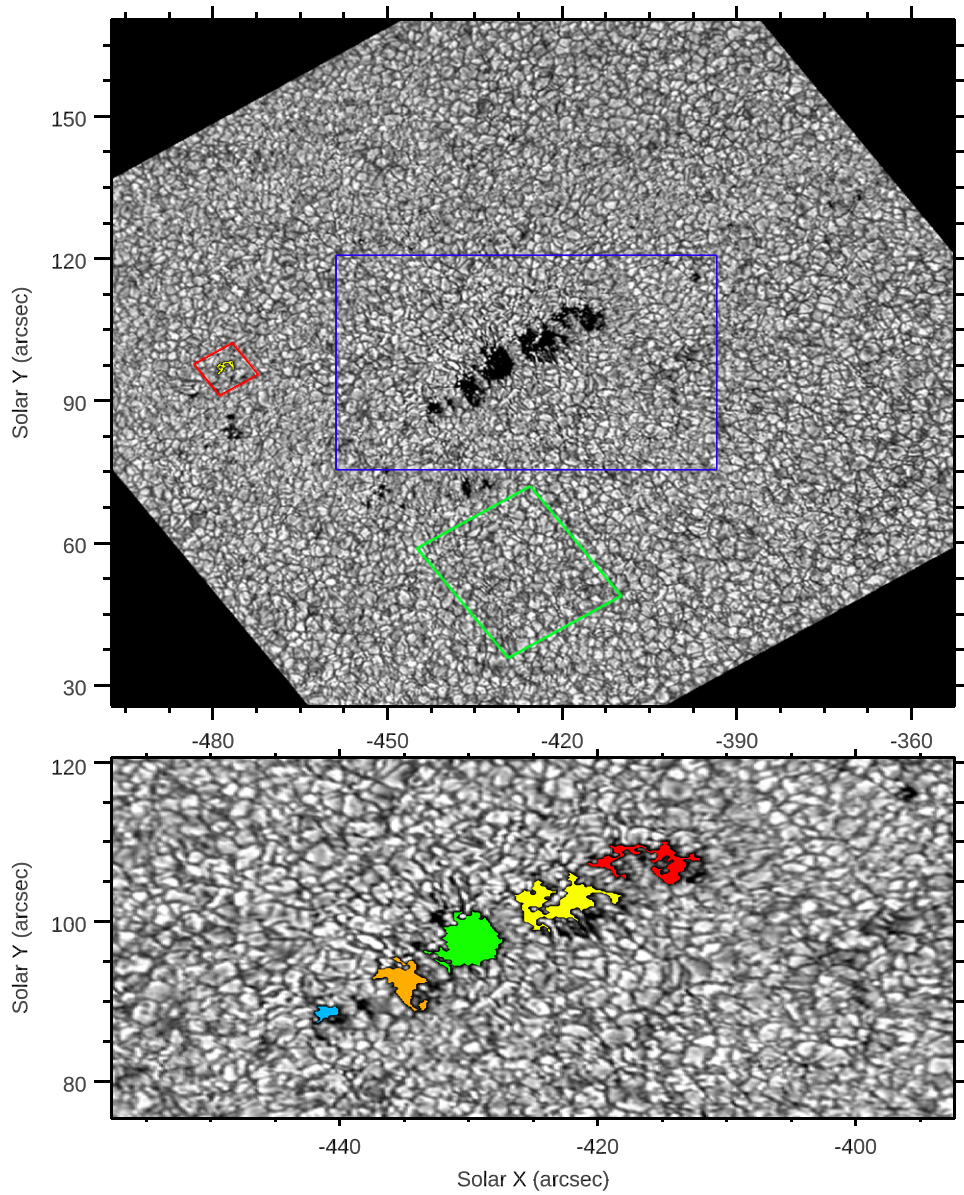
Figure 1. The upper panel displays a 4170 Å continuum image of the full ROSA field of view in proper heliocentric coordinates. The green box outlines the quiescent region used for the calculation of intensity thresholds that are used to define the pore boundaries, the blue box highlights the region of interest displayed in the lower panel, and the red box contains the reference magnetic structure (yellow). The lower panel shows the five pores, labeled in ascending order from left to right, with pore 1 (P1) being blue, pore 2 (P2) orange, pore 3 (P3) green, pore 4 (P4) yellow, and pore 5 (P5) red.

deviation, σ, at each time step. The pores were then identified individually as significant clusters of pixels within the reduced field of view exhibiting less intensity than a threshold of $I_{mean} - 2.5\sigma$. Due to the dynamic evolution of small-scale magnetic flux in the active region, a minimum size threshold of 50 pixels ($\sim$630,000 km^2) was placed on identified pixel groupings, with any objects below this excluded. This had the effect of underrepresenting the perimeter of pore five on occasion, as it branches into two objects for a short period due to convective buffeting. However, it is of greater importance to retain only the pixels that definitely constitute the five pores in order to ensure any detected oscillations are being channeled by the larger flux tubes (i.e., minimizing any wave contributions from neighboring nonpore photospheric plasma). The average areas of the pores (henceforth referred to as P1–P5; see Figure 1 for their specific labels) were calculated and are presented in Table 1, confirming that the active region was

configured as two large central pores, P3 and P4, bounded by smaller pores, P1, P2, and P5.

The identification of pore boundaries allows for the extraction of plasma characteristics to confirm the existence of sausage-mode oscillations. Following the methodology of Moreels et al. (2013), time series of area, Lagrangian (total) intensity, and Eulerian (average) intensity were calculated for each pore. Morlet wavelet analysis (Torrence & Compo 1998) was utilized to infer information on quasi-periodic signals, with each time series first detrended using a linear line of the best fit and mean normalized. As seen in Figure 4, significant quasi-periodic oscillatory power was found in the 3–5 minute period band, peaking at $\sim$210 s (4.76 mHz) for each pore in both intensity and area, consistent with the solar photospheric p-mode spectrum (Lites et al. 1982) and previous reporting from GM21.
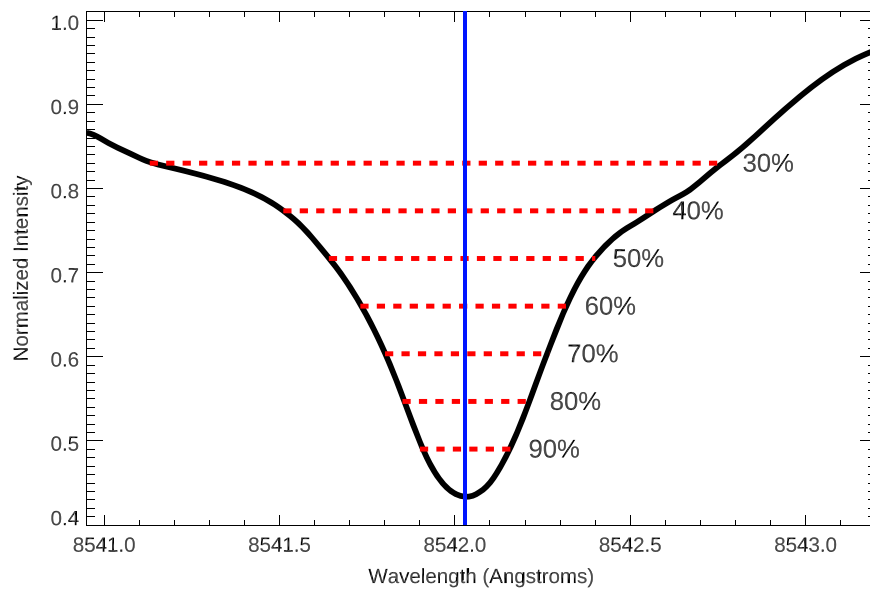
Figure 2. Temporally and spatially averaged Ca II 8542 Å profile for the full field of view (including pores, small-scale magnetic elements, and quiet-Sun locations). The blue line illustrates the calculated line core for these observations (8542.03 Å), with the red dashed lines highlighting the percentage line depths used to calculate the corresponding bisector velocities.
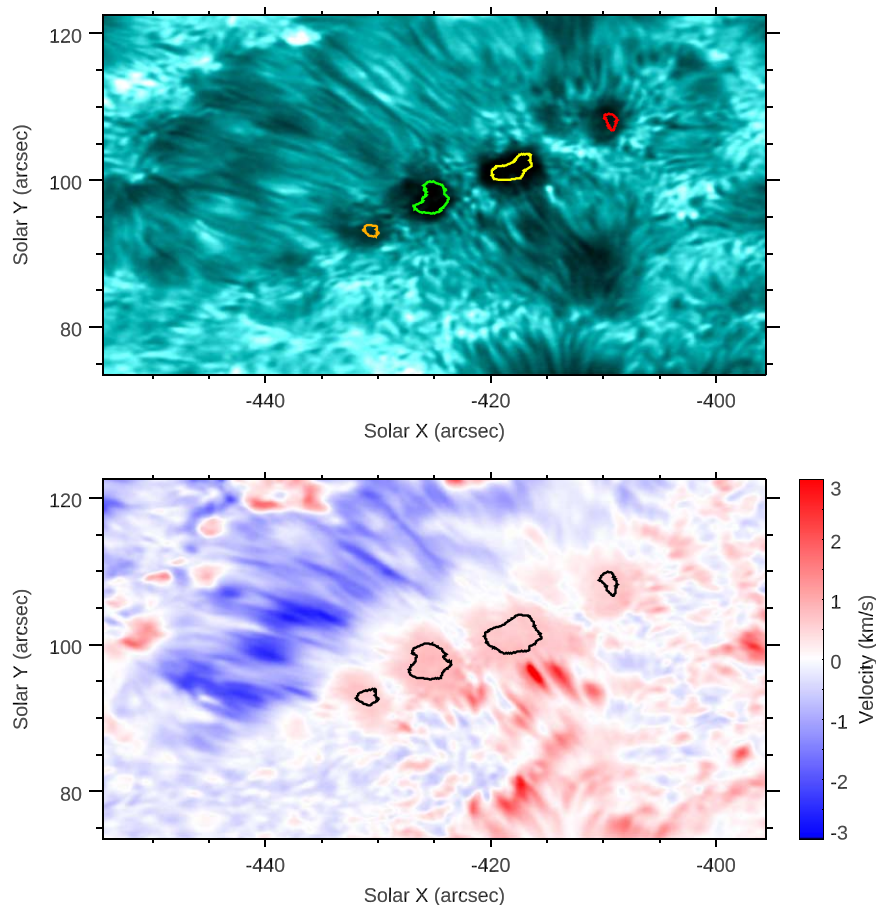

Figure 3. The upper panel displays a typical IBIS line-core (8542.03 Å) image of the pores in true heliocentric coordinates. The time-averaged perimeters of the established pore boundaries across the bisector range are contoured in the same color scheme as Figure 1. The lower panel shows the average line-core line-of-sight velocity of the same region, where a positive value is a plasma downflow (i.e., redshift), with the time-averaged pore perimeters at the line core contoured in black.

The identification of perturbations in the area of the pores denotes compressible sausage modes, the form of which can be confirmed by assessing the phase relationship between area and Lagrangian intensity oscillations (Moreels et al. 2013). Wavelet phase analysis was utilized (Torrence & Webster 1999), with only common oscillations in both time series exhibiting a lifetime greater than $\sqrt{2}\, P$, where P is the period of the wave,

Table 1
Properties of the Five Pores Identified in GM21 at A Height of ∼25 km

Parameters	Pore 1	Pore 2	Pore 3	Pore 4	Pore 5
Magnetic Field (kG)	1.49 ± 0.12	1.58 ± 0.16	1.68 ± 0.19	1.68 ± 0.21	1.49 ± 0.11
Temperature (kK)	5.67 ± 0.07	5.34 ± 0.28	5.18 ± 0.28	5.20 ± 0.23	5.48 ± 0.14
$\mathrm{Log_{10}}$ Density (kg/m^3)	-3.19 ± -4.75	-3.15 ± -4.25	-3.13 ± -4.24	-3.13 ± -4.35	-3.17 ± -4.51
Area (Mm^2)	1.1 ± 0.03	5.88 ± 0.8	12.01 ± 0.8	11.73 ± 0.7	7.5 ± 0.3
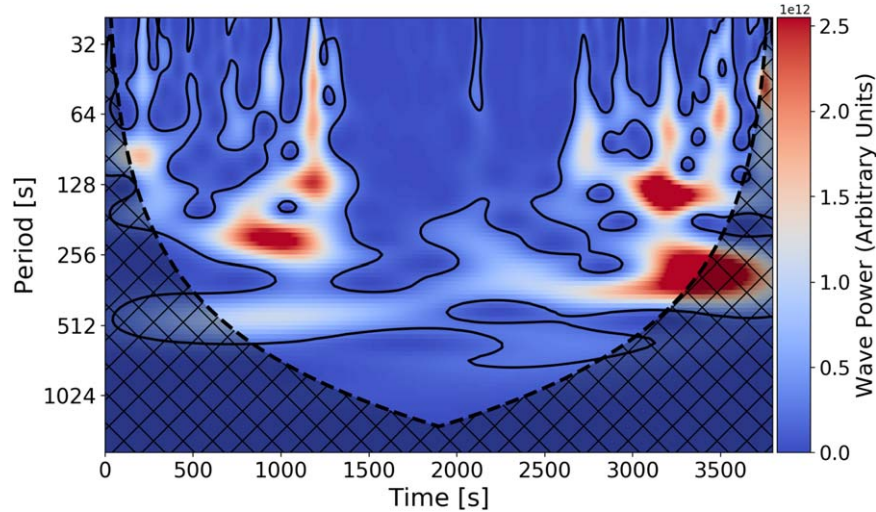
Figure 4. Wavelet power spectrum of the cross-sectional area time series of P3 from the 4170 Å ROSA continuum filter. The contoured region are those regions calculated to be above the 95% confidence of containing coherent oscillatory power. The hatched region to the bottom of the figure represents the cone of influence.

and a normalized cross-correlation coefficient greater than 0.5 considered, encompassing the wave power above the 95% confidence interval (Torrence & Webster 1999; Grant et al. 2015). These steps were taken to ensure that detected signals were periodic and were indeed the same perturbation being considered in both time series. For each pore, a strong in-phase relationship between the area and Lagrangian intensity is found, with the relative phases being close to 0°. For each pore, the phase difference between the area and Lagrangian intensity is: $P1 = -2°.61 \pm 4°.23$, $P2 = -2°.65 \pm 3°.07$, $P3 = -2°.21 \pm 2°.27$, $P4 = -0.16 \pm 1.18$, and $P5 = -1°.49 \pm 1°.72$. The strength of this in-phase behavior confirms the existence of slow-mode sausage waves in every magnetic structure (Moreels et al. 2013), corroborating the conclusions of GM21, and further supporting the ubiquity of sausage modes in photospheric pores (Keys et al. 2018).

The classification of compressible MHD waves in each pore naturally leads to the study of whether these modes are exclusive to each structure, or exhibit a coherency across the active region. This was initially conducted through wavelet phase analysis of the area, Lagrangian, and Eulerian intensity time series between adjacent pores, using the same criteria previously determined. The phase difference between the structural oscillations of the pores are documented in Table 2 and reveal a definite commonality between the pores, with every oscillatory property exhibiting phases centered around zero degrees. This observed coherence is indicative of a common wave driver acting on each structure in unison and provides a novel configuration where waves with equivalent initial properties can be studied across differing magnetic structures. In order to confirm such an assertion, further analysis was necessary to assess the coherency of perturbations across the entire field of view.

Table 2
Phase Relationships of Oscillatory Properties between Adjacent Pores

Pore Comparison	Area (°)	Lagrangian (°)	Eulerian (°)
Pore 1–2	1.05 ± 2.71	0.95 ± 1.51	-1.09 ± 1.66
Pore 2–3	-1.14 ± 2.43	-1.05 ± 1.27	-0.22 ± 1.21
Pore 3–4	-2.35 ± 2.56	0.06 ± 0.88	2.67 ± 0.89
Pore 4–5	3.72 ± 2.59	1.52 ± 1.32	-0.42 ± 0.67
Pore 1–5	-0.59 ± 3.45	1.27 ± 1.61	0.86 ± 1.12

First, a statistical study of the relationship between intensity oscillations in neighboring pores was undertaken on a pixel-by-pixel basis. In order to extract a large sample of representative intensity time series from within the pore boundaries for analysis, the identification of pixels corresponding to locations that exist within the time-dependent pore perimeters at all times was necessary. This was achieved through the coaddition of binary maps of the pores across all times, where in each imaging frame the pore structures were given a value of "1", and all other locations were set to "0". Once normalized by the number of images, the locations equal to 1 were extracted for investigation. Due to the morphology of the pores throughout the observing time in this decaying active region, the subsets of "constant" pore pixels represent fractions of the total pore areas, with the natural exclusion of pixels at the perimeters of the pores, which are the most impacted by any shifts introduced by seeing effects or the techniques used to correct them. For each of the pores, the number of pixels in this subset, alongside the value quantified as the percentage of the total pixels that fall within their boundaries are as follows: $P1 = 22$ (25%), $P2 = 198$ (43%), $P3 = 472$ (50%), $P4 = 379$ (41%), and $P5 = 126$ (21%).
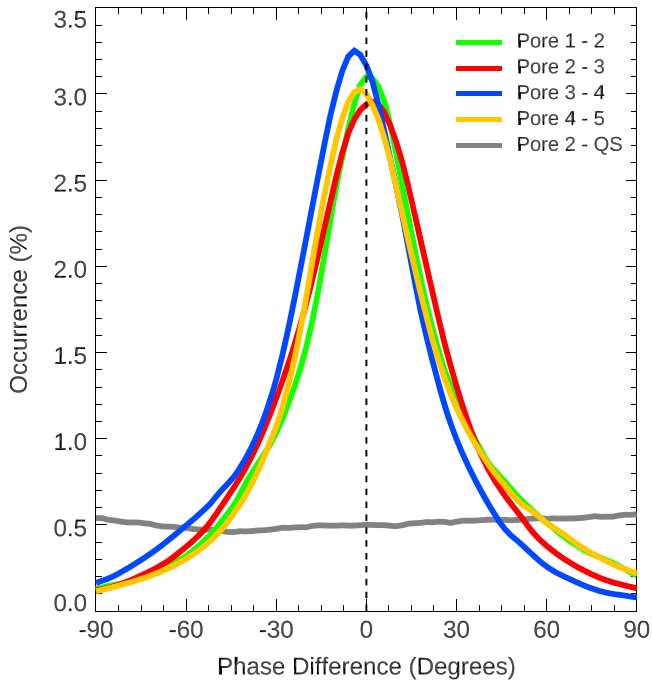
Figure 5. Histograms of the phase differences between coherent oscillations within pixels of adjacent pores. The dashed black line represents a phase lag of zero degrees. The histogram of P1–P2 is in green, P2–P3 in red, P3–P4 in blue, P4–P5 in yellow, while the comparison between P2 and a quiet-Sun region is displayed in gray.

The coherency of adjacent pore oscillations was probed through further wavelet phase analysis, whereby every pixel in a pore was analyzed with respect to every pixel in its adjacent pore. This provided a large sample of distinct phase calculations, for instance, in the case of P3–P4, 178, 888 individual phase relationships were calculated. Every phase angle value that corresponded to the previously outlined criteria were then collected, with $\sim 10^8$ extracted phase results in each case. The results of each study are visualized as histograms in Figure 5, where they display a Gaussian-like distribution, with clear dominant peaks around zero degrees, with the most prominent phase differences manifesting at: P1–P2 $= 1°\!\!.08$, P2–P3 $= 1°\!\!.67$, P3–P4 $= -5°\!\!.45$, and P4–P5 $= -5°\!\!.62$. The direct comparison of distinct regions (e.g., a central and perimeter pixel) in adjacent pores leads to a larger range of observed phase angles, where small deviations away from zero degrees due to compositional differences in the plasma column (affecting the associated optical depths), in addition to the Wilson effect (Wilson & Cannon 1968), are likely. Despite this, the coherence of waves across the pores has been corroborated by the clear display of similarly shaped distributions, alongside associated dominant phase lags approaching zero degrees.

Further analysis was necessary to ensure the distributions in Figure 5 were neither a statistical effect, spurious information added through instrumental noise, such as the uncorrected tail of the point-spread function (PSF) of the telescope (Marino et al. 2006) nor atmospheric turbulence (Rimmele 2004). Two processes were undertaken to verify the derived relationships in Figure 5. First, wavelet phase analysis was conducted between the pixels in P2 and the quiet-Sun region outlined by the green box in Figure 1. The consideration of a region free of strong magnetic flux and distant from the active region will confirm the uniqueness of the commonality of waves in the pores, with

the influence of the PSF limited to its FWHM and the isoplanatic patch caused by turbulence tending to $\sim 5''$–$10''$. Common periodicities of the embedded wave activity are found between the pore and quiet-Sun region, as to be expected as a result of ubiquitous photospheric p-mode generation. Critically, the resulting phase distribution, visualized by the gray line in Figure 5, shows no preferred phase lag, with all values being approximately likely. The lack of any discernible relationship between these regions infers that the commonality of the pores is not due to any instrumental effects. However, it is also prudent to confirm that the pore relationship is not influenced by seeing effects, such as stray-light enhancements of dark regions, or the reconstruction techniques used to correct for them. This was conducted through a comparison of P3 with a small magnetic structure separate to the cluster of pores (as seen in Figure 1). This feature is noticeably smaller than the pores under study, with its perimeter contoured by a threshold of $I_{\mathrm{mean}} - 1.5\sigma$. This made the object more transient in nature, with significant morphological and location changes across the observing window. As a result, no pixels that contained consistent magnetic plasma throughout the time series could be identified, prohibiting a statistical study as seen in Figure 5. Instead, wavelet analysis of the average emergent intensity of this structure and P3 was conducted and is displayed in Figure 6. From inspection, there are limited points in the time series where the two structures share common oscillations, and mostly at higher frequencies than those associated with global p-modes. It is also clear that those correlated periodicities are not in-phase, with an average phase angle of $-93°\!\!.8 \pm 104°\!\!.2$ from those regions above the 95% confidence interval, with the larger range of observed values likely being influenced by the introduction of perimeter pixel measurements and their associated uncertainties as discussed above. The comparison with a separate magnetic structure has shown that there are negligible effects on the coherent nature of the waves in the pores due to any effects across the field of view. It has also shown that the tails of the distributions in Figure 5 are likely caused by the high-frequency, antiphase spurious signals seen in Figure 6, strengthening the validity of the peaks around zero degrees. These analysis steps further verify that the negligible phase lags observed between adjacent pores are a real effect and confirm the commonality of the wave driver within the five pore structures.

The ubiquitous p-mode waves seen across the photosphere are generated in the subsurface convection zone, through the entropy fluctuations and Reynolds stresses associated with the mixing of magnetic fields and turbulent plasma (Nordlund & Stein 2001; Stein & Nordlund 2001). The excitation of p-modes appears to be most prominent just below the interface between the convection zone and the solar surface, where the perturbations in convective plasma parameters are largest (Nordlund et al. 2009). The driver itself can manifest as either a localized force, or as an extended force across a large plane. The observations presented here would indicate the latter, given the coherence of waves across multiple pores spanning tens of megameters. However, the results of Riedl et al. (2021) offer a contrasting view. In their two-dimensional simulations of P3, an extended driver across the lower boundary of both the pore and neighboring quiet Sun could not replicate the damping seen in GM21, and in fact produced an increase in the wave energy flux with height. Instead, they found good correlation with the observations of GM21 through the application of a localized
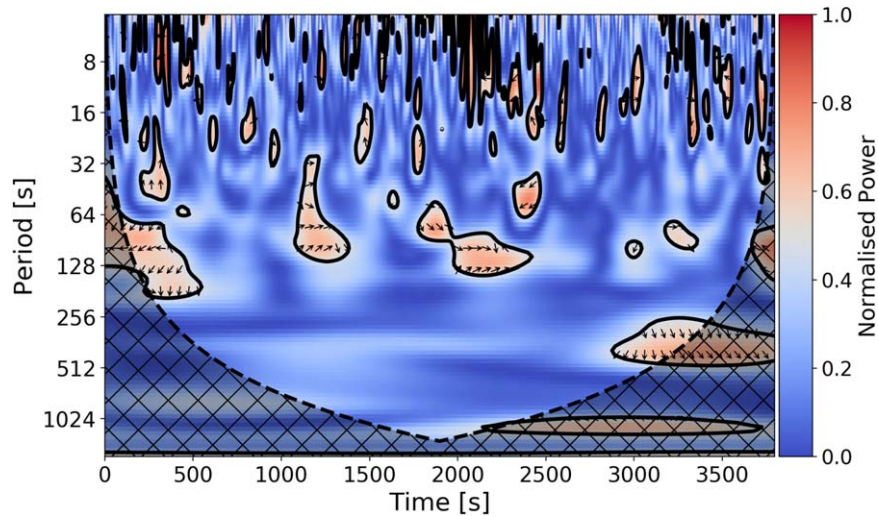
Figure 6. Normalized cross power spectrum from the wavelet analysis between the average intensity emission of P3 and reference magnetic feature. Contoured regions represent the values above the 95% confidence interval, with the phase angle between the time series represented by arrows (a 0° phase lag is represented by an arrow pointing right, 180° by a left arrow, and 90° and −90° by up and down arrows, respectively). The cone of influence is represented by the hashed region.

driver within the pore. This scenario, where each pore has a distinct, localized driver acting upon it to produce equivalent oscillations is unlikely, as the frequency distribution of generated waves in the convection zone is dependent on both the magnetic field strength and inclination of flux tubes (Jacoutot et al. 2008; Kitiashvili et al. 2011). Instead, it appears more likely that the waves must be generated at a lower height in the convection zone where the emerging flux bundle is monolithic, before it separates into smaller fragments, manifesting at the surface as the magnetic pores (e.g., Zwaan 1985; Cheung et al. 2010; Chen et al. 2017). This scenario allows for each pore in the photosphere to exhibit an identical distribution of MHD oscillations, and thus provides a unique opportunity to study the development of equivalent perturbations in differing waveguides into the chromosphere.

3.2. Chromospheric Propagation

The Ca II 8542 Å line was employed to study the pores as they branch into the chromosphere. This spectral line has been a key chromospheric observable for decades and will be a key diagnostic for multiple instruments at next-generation observatories such as the Daniel K. Inouye Solar Telescope (DKIST; Rimmele et al. 2020; Rast et al. 2021). The collection of high-cadence spectral scans of this line allowed Doppler velocity signatures to be employed as an additional diagnostic of the pore oscillations. The introduction of Doppler velocity data is necessary, as previous studies have established that chromospheric wave fronts, manifesting as notable line-core intensity brightenings, can propagate across a significant proportion of a pore's surface area at a given time in Ca II 8542 Å observations (e.g., Cho et al. 2015). These umbral wave fronts therefore negate time-dependent intensity thresholding of the pore perimeters, and prohibit the measurement of chromospheric area perturbations. Instead, the line-of-sight (LOS) velocity (v_{LOS}) of the plasma is inferred for each pixel, with the time-averaged line-core v_{LOS} for the field of interest displayed in the lower panel of Figure 3.

When seeking to identify the propagation of MHD waves in the solar atmosphere, multiline observations are often used in concert to ascertain phase lags (e.g., Giovanelli et al. 1978;

Lites 1984; Centeno et al. 2006). In this study, the Ca II 8542 Å spectral line is the only chromospheric observable; thus it is prudent to investigate whether the propagation characteristics of MHD waves can be ascertained from single-line observations of Ca II 8542 Å through the derivation of bisector velocities.

3.2.1. Ca II 8542 Å Bisectors

The technique of inferring v_{LOS} from various bisectors across a spectral line to provide height-stratified information is commonly used for photospheric lines (Kulander & Jefferies 1966; González Manrique et al. 2020), such as Si I 10827 Å in the case of GM21, due to their symmetrical profiles. However there are only few examples of inferring Ca II 8542 Å bisector motions in magnetic flux tubes (e.g., Chae et al. 2013; Beck & Choudhary 2020), due to a range of chromospheric effects capable of adding nonlinearities to the absorption profile. Therefore it was prudent to first ensure the spectral profiles within the pores were suitable for bisector analysis. This was achieved through use of the Multi-Component Atmospheric Line Fitting program (MCALF; MacBride & Jess 2020; MacBride et al. 2021; MacBride & Jess 2021), in particular the efficient machine-learning scheme that classifies Ca II 8542 Å profiles into five categories based on the degree of line-core emission. MacBride et al. (2021) highlight that category three (or above) is a result of substantial emission within the line profile, and hence are unsuitable for bisector analysis. Thankfully, only classification categories 1–2 were found within or around the vicinity of the pores. This both establishes that the pore observations are suitable for bisector analysis, and that none of the wave power detected in the photosphere is being dissipated through detectable shock formation, as the pores lack the associated line-core brightening (Grant et al. 2018). This does not imply that nonlinearities are absent in the pores. The atmosphere of a shock contained within an observed pixel has long been established to have two-components, impulsive and quiescent (Socas-Navarro et al. 2000). The detection of the shock is therefore dependent on the filling factors of these components and implies that shocks can form below the resolution of current instruments. Given the

diversity and complexity of geometric configurations that pores can display (e.g., Sobotka 2003), the gradients in density and magnetic field necessary to steepen waves into shocks can manifest in pores. Therefore, any future study of pores in Ca II 8542 Å must continue to confirm that no discernable emission in the core of the line is present.

Bisectors were calculated at locations representing 40%–90% of the line depth relative to the measured average line center of the data (8542.03 Å), in intervals of 10% (see Figure 2). The resulting bisector velocity is a measurement of the shift in wavelength of the Ca II 8542 Å line wings at these positions and was conducted for all profiles in the field of view. For this data set, only bisectors as low as the 40% line depth were used, as isotopic splitting of the Ca II 8542 Å line produces an asymmetric profile, with a redshifted "inverse-C" shape causing uncertainty at wavelengths far from the line center (i.e., in the 10%–30% line-depth interval; Uitenbroek 2006; Leenaarts et al. 2014). In addition to central reversals from shocks, nonlinearities can be introduced to the absorption line through density enhancements in the lower atmosphere. As shown in Carlsson & Stein (1997), the emission source function is coupled to the Planck function in the high photosphere. As a result, density changes in this region produce notable brightening in the blue wing of the profile, resulting in what would appear to be the redshifted signature of a downflow (see further discussion in Henriques et al. 2020). The erroneous introduction of a broad redshift due to localized upflows have already been confirmed due to shocks (Henriques et al. 2017) and flares (Monson et al. 2021). Despite no signatures of these impulsive events within the pores observed here, incremental density excursions may skew the derived bisector velocities; thus inspection of the derived velocities for this effect is necessary.

In order to study the pore oscillations across the derived bisector velocities, the chromospheric pore perimeters must be established. The lesser contrast between pores and the quiescent background in the chromosphere necessitated the use of time-averaged images of the field of view, in order to better isolate the pore boundaries. In addition, from inspection of the data (see the upper panel of Figure 3), it is clear that P1 is not obviously detectable, which is indicative of either the similar chromospheric temperature profiles of small pores to the quiescent background, or the rapid expansion and volume filling of the magnetic fields (Solanki et al. 2017). As a result, pore P1 was excluded from any further study in the Ca II 8542 Å line. To ensure pore perimeters were valid across every line depth used, a summed wavelength image, spanning ± 0.54 Å relative to the line core, which encompasses the 40% line-depth region, was generated. The pore thresholding was conducted in an identical manner as described in Section 3.1, but with bespoke thresholds for each pore, given the variable connectivity between certain pores and dark fibrilar structures. The selected thresholds were: $P2 = I_{\mathrm{mean}} - 2.28\sigma$, $P3 = I_{\mathrm{mean}} - 2.82\sigma$, $P4 = I_{\mathrm{mean}} - 2.84\sigma$, and $P5 = I_{\mathrm{mean}} - 2.04\sigma$, which are used to contour pores P2–P5 in the upper panel of Figure 3.

The bisector velocities for P3 are plotted in Figure 7 and are representative of the other pores. It can be seen that there is a small redshifted average of between 0.64 and 0.81 km s^{-1} (seen in Figure 3). However, it is not certain that this is not caused by an upwardly propagating (i.e., blueshifted) density enhancement in the lower atmosphere, as chromospheric downflows have also been associated with rapid cooling within the interior of the pores in the lower atmosphere (Steiner et al. 1998; Kato et al. 2011; Cho et al. 2013). The lower panels of Figure 7 show the distribution of velocities on a pixel-by-pixel level for pore P3 at 50% and 100% (line core) line depths. The 50% line depth was selected to exhibit the full bisector range, as from inspection of the top panel the 40% line-depth bisector displays a larger variance, likely due to the influence of the previously mentioned "inverse-C" effect. It can be seen that in both samples, there is a predominant trend around the average and an approximately normal distribution, with excursions at the tail on the order of 1%. This further reinforces that, for this data set, any skewness as a result of localized density enhancements in the photosphere are minimal, as consistent and expected behavior is seen within the LOS velocity samples at a range of line depths.

To gain insight into the differences in atmospheric heights sampled by the bisectors, the response function of the Ca II 8542 Å intensities (Stokes I) is considered. The response function describes the sensitivity of emergent intensity to changes in temperature as a function of the height and wavelength. The response of the Ca II 8542 Å line has been analyzed for quiescent parts of the solar atmosphere (e.g., Cauzzi et al. 2008). However, the effects on sensitivity within a strongly magnetic atmosphere has yet to be investigated. To probe the response of the line to pore-like magnetism, the warm sunspot umbral model "L" of Maltby et al. (1986) was employed, with the responses of the spectral line calculated according to the method of Fossum & Carlsson (2005b). In this method, the atmospheric model is perturbed successively at each height in temperature by 1% with a step function that is unity from the lower atmospheric boundary to the depth point under consideration, and zero above that. For each perturbation, the change in intensity, ΔI_λ, is recorded and the response function is derived by calculating the derivative of $\Delta I_\lambda / I_\lambda$ with atmospheric height. The output of this process is plotted in the left panel of Figure 8, showing the photospheric nature of the Ca II 8542 Å wings and the higher chromospheric heights sampled toward the line core.

For reference, the responses of the line-depth locations for the reference profile in the left panel of Figure 8 are calculated and visualized as a cumulative response function for each percentage line depth (top right panel of Figure 8) and as a cumulative distribution function (CDF) of the total line-depth responses (lower right panel of Figure 8). The response function shows that the bisectors are indeed sampling iteratively higher heights in the solar atmosphere as a function of the line depth. However, the CDF shown in the lower right panel of Figure 8 implies that the bisectors still have a considerable contribution from the lower atmosphere, with only wavelengths close to the line core deviating in its development through the atmosphere, providing a notably more purely chromospheric response.

With the response to emergent intensity derived, the response of the Ca II 8542 Å line to velocity perturbations can also be calculated. The same atmospheric model is used as depicted in Figure 8; however, in this occasion a constant 1 km s^{-1} upflow velocity is applied across the atmosphere and subsequently perturbed by 1%. The resulting intensity change is displayed in Figure 9, with positive response values indicating an intensity increase, while the negative values denote an intensity decrease. From inspection, the effects of a
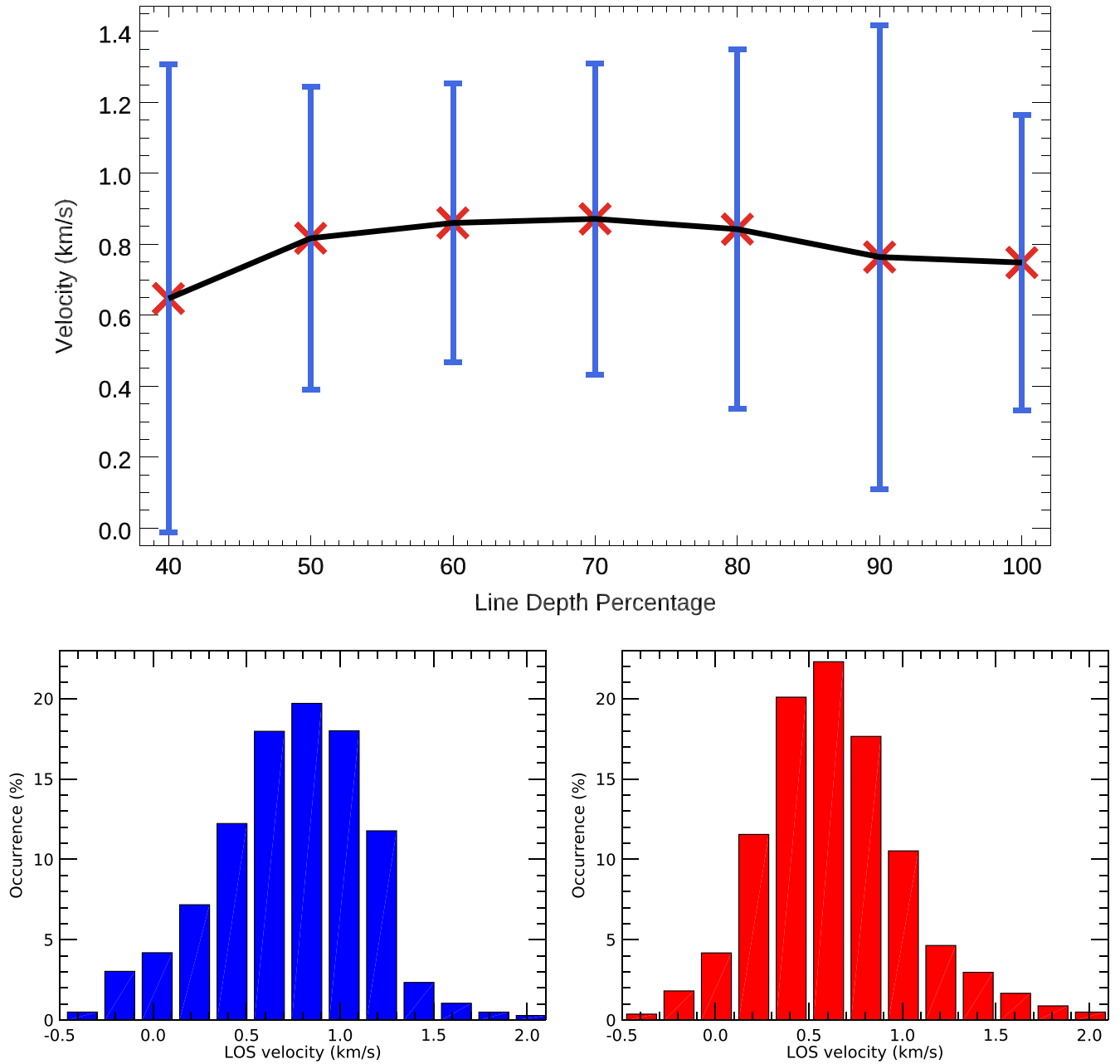
Figure 7. Top panel: Average LOS velocity for P3 at each percentage line depth, with standard deviations plotted for each measurement. Bottom panels: Histograms of the LOS velocities of the pixels contained within the P3 contour spanning the full height range of measurements. The left panel (blue bars) represents the velocities at 50% line depth, while the right panel (red bars) displays the line-core velocities calculated at a 100% line depth.

velocity oscillation are predominantly seen in the chromosphere, as expected, and subtend a range of wavelengths around the line core. This implies that there will be a measure of integration of chromospheric velocity signals at these wavelengths. The influence of photospheric velocity perturbations are limited to small portions of the wing, where they will provide a component of integrated response at those wavelengths. However, the strong photospheric contributions seen in Figure 8 are not equivalently present in Figure 9, indicating that the large photospheric contributions in the temperature response functions may be overestimated, especially given the lack of photospheric granulation in the top panel of Figure 3. Therefore, it is prudent to test the accuracy of the derived responses, which can be achieved through investigation of pore wave power as a function of the frequency throughout the

individual line depths. Of particular interest is the cutoff frequency, resulting from the influence of gravity on wave propagation, leading to smaller frequencies being unable to propagate to higher heights (Bel & Leroy 1977). Various models predict that the cutoff frequency is a height-stratified quantity, with previous attempts made to constrain the atmospheric heights at which these cutoffs manifest (e.g., Schmitz & Fleck 1998). However, dependencies on quantities such as the magnetic field strength and inclination angles make it difficult to produce a unified height model (Centeno et al. 2009; Felipe & Sangeetha 2020). What is clear from observations is the dominance of five-minute periods in the lower photosphere, to heights of at least ∼400 km (Felipe et al. 2018; Rajaguru et al. 2019), before these periods are unable to bridge into the chromosphere, allowing three-minute
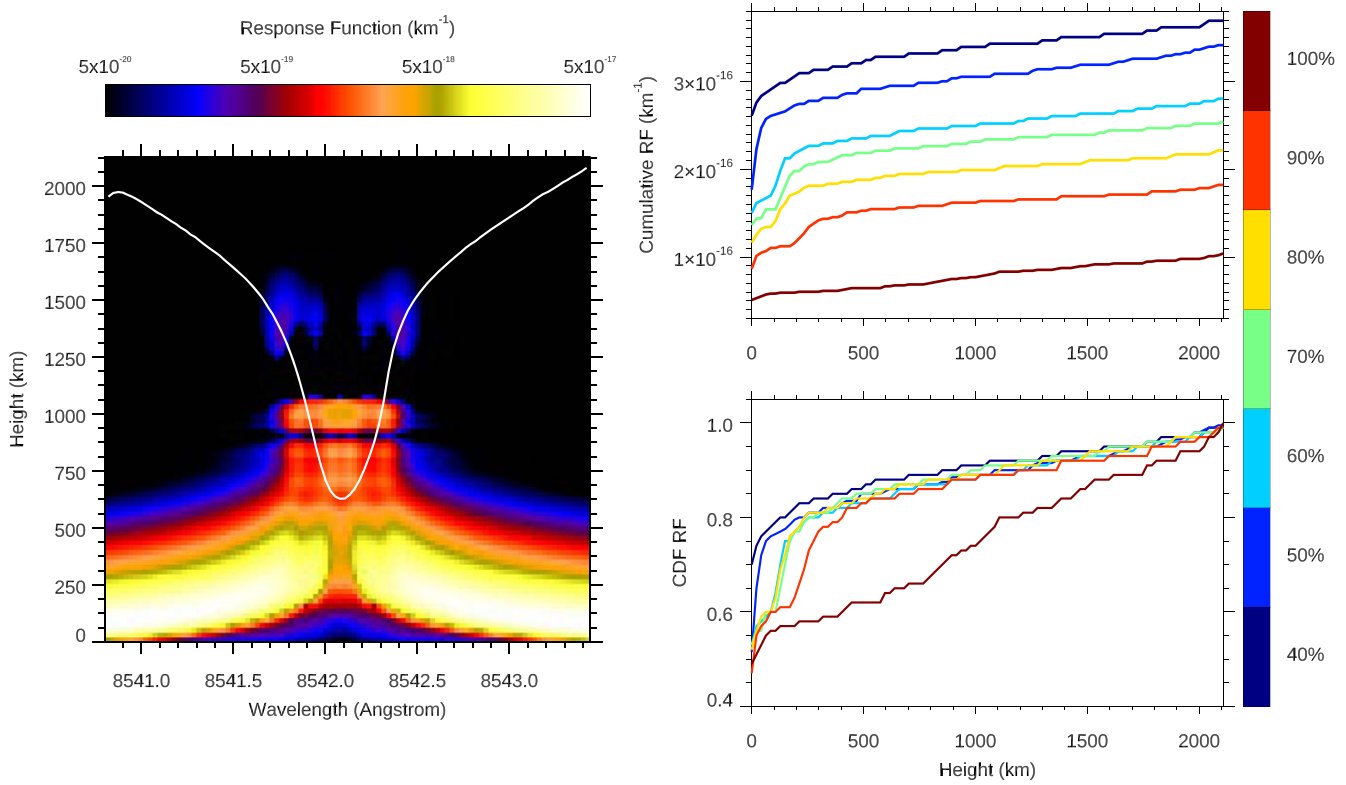
Figure 8. Left panel: Response function of the Ca II 8542 Å spectral line to temperature perturbations in a magnetic atmosphere, with a Ca II 8542 Å reference profile plotted in white. Upper right panel: Cumulative response function with the height, measured at the wavelengths corresponding to each line depth, which are colored according to the legend on the right. Lower right panel: Cumulative distribution function of each bisector response function, with the same color key as above.
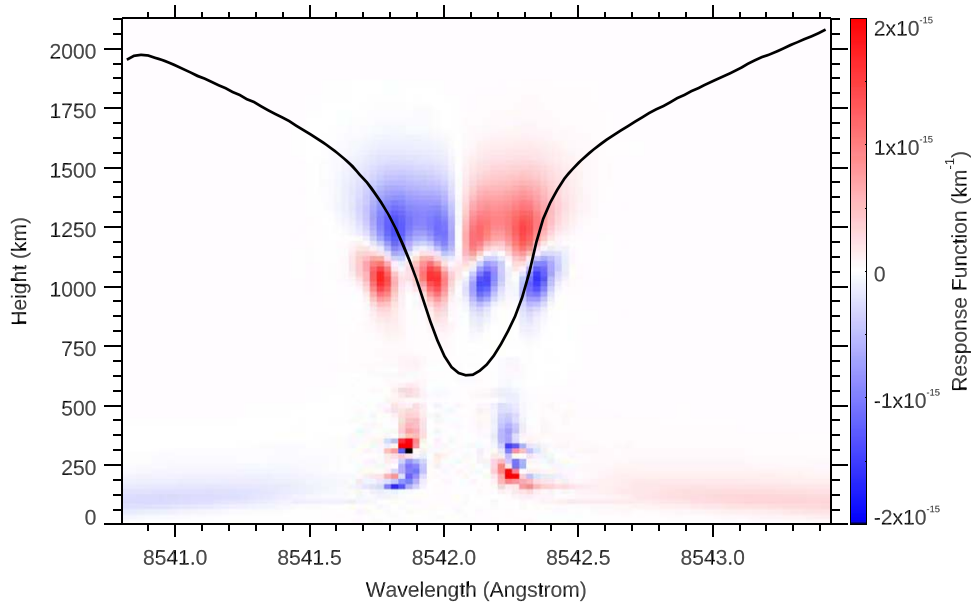

Figure 9. Response function of the Ca II 8542 Å spectral line to a 1 km s^{-1} velocity perturbation in a magnetic atmosphere, with a Ca II 8542 Å reference profile plotted in black. Positive (red) values refer to an intensity brightening as a result of the perturbation, with negative (blue) values referring to a reduction in intensity.

oscillations to become prominent (Centeno et al. 2006; Wiśniewska et al. 2016). Therefore, assessment of the photospheric contributions to Ca II 8542 Å bisector formation can be examined through the gradual rise of lower-frequency wave power as the percentage line depth sampled becomes smaller.

Using the established pore perimeters, the spatially averaged velocity time series for each of the percentage line depths were isolated for inspection. It was immediately apparent that for all

bisectors, the 5 mHz (3 minute period) frequency was prominent across all pores. However, Fourier power is a relative quantity, dependent on many factors of the observations, and often normalized to inhibit direct comparison. For a more robust measure of wave activity throughout the bisectors, the energy spectral density was calculated for each time series, where its normalization is relative to the frequency resolution of the time series (i.e., providing a "per mHz" quantity) allows
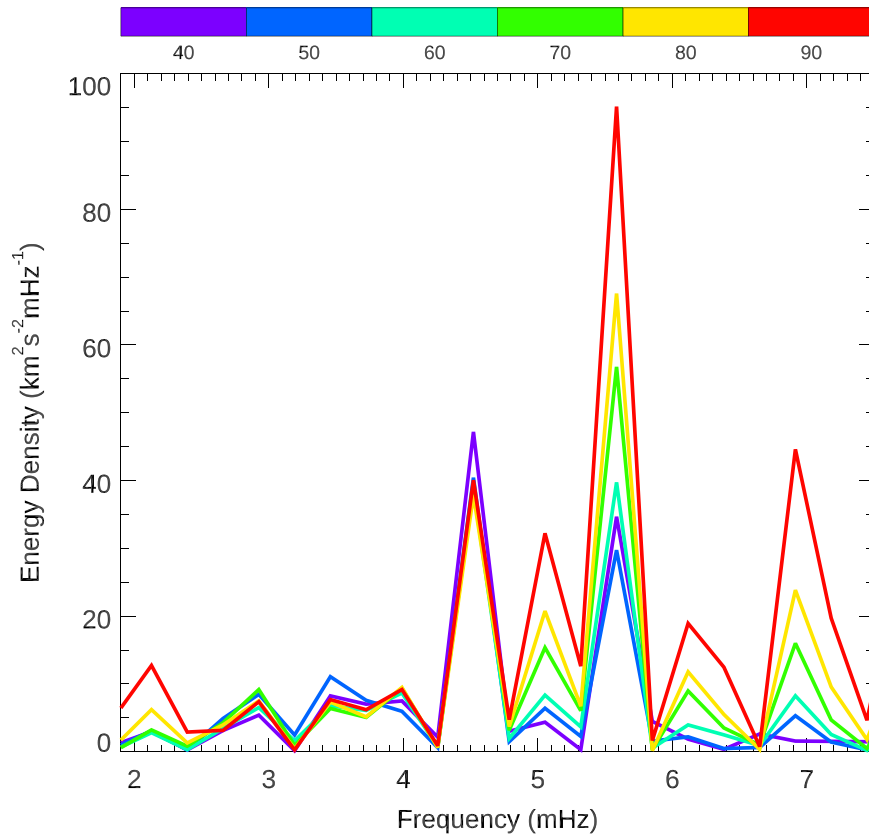
Figure 10. Energy spectral density of the spatially averaged bisector velocities from pore P3, plotted in a color scheme represented in the legend above, where the unit corresponds to the percentage line depth of the Ca II 8542 Å line.

for future direct comparison between different observing regimes. The energy spectral density, S, is defined following the convention described by Stull (1988),

$$S = \frac{2 \, |X(f)|^2}{\delta \nu}, \quad (1)$$

where $X(f)$ is the Fourier power spectrum of the time series, and $\delta \nu$ is the corresponding frequency sampling.

The spectral energy densities for pore P3 are shown in Figure 10 for inspection. It is clear that the ∼3 mHz photospheric contribution is not present in any of the bisector velocities, indicating that the cutoff height is below that sampled by the 40% line depth. In contrast, the ∼5 mHz chromospheric oscillation is prominent across all 40%–90% line depths, with a shift in the dominant frequency found throughout the line depths, from ≈4.5 mHz (221 s) at 40%, to a peak at ≈5.6 mHz (179 s) for 90%. As such, the derived bisector velocity time series provides observational evidence of the gradual enhancement of three-minute wave power as the waves propagate through to higher chromospheric heights.

In the case of pore P3, the ≈5 mHz spectral energy density increases incrementally by a factor of 2 across the range of 40%–90% of the Ca II 8542 Å line depth, and in the case of ≈7 mHz by a factor of 10. Simulations have highlighted the amplification of higher-frequency (≥5 mHz) power as the waves propagate through negative density gradients (Khomenko & Collados 2015; Felipe 2019), and although previous observational studies have identified the shift in dominant power (e.g., Krishna Prasad et al. 2015), they lacked the height sampling necessary to track this gradual increase in wave

power through the chromosphere. The fidelity of the measured wave enhancement shown in Figure 10, allied with the shift in dominant frequency, shows that despite the influence of photospheric heights in the Ca II 8542 Å response functions (see, e.g., the left panel of Figure 8), the bisector velocities are capturing signals from progressively higher chromospheric heights as a function of the line depth. This provides confidence in the capability of bisector Doppler velocity analysis to resolve wave signatures in the chromosphere without the strict need of multiline observations, and allows for an investigation of the development of the coherent pore oscillations as they move into the chromosphere.

3.2.2. Interpore Coherency

Initial consideration was focused on whether the oscillations within each pore retained their photospheric coherence, i.e., remained in-phase with one another as they propagated into the chromosphere. Given the suppression of lower p-mode frequencies in the chromosphere, Fourier analysis was employed in the study of coherent wave signatures in order to provide better resulting frequency resolution, without the convolution effects of wavelet analyses. For this analysis and comparison between multiple time series at shared coherent frequencies, a 95% confidence threshold was set as a baseline requirement for positive frequency detections.

The Ca II 8542 Å line-core region was investigated as it probes the highest average chromospheric heights and provides the greatest contrast from the region studied in Section 3.1. To achieve this, bespoke pore perimeters were established from 8542.03 Å images, with selected contouring thresholds of
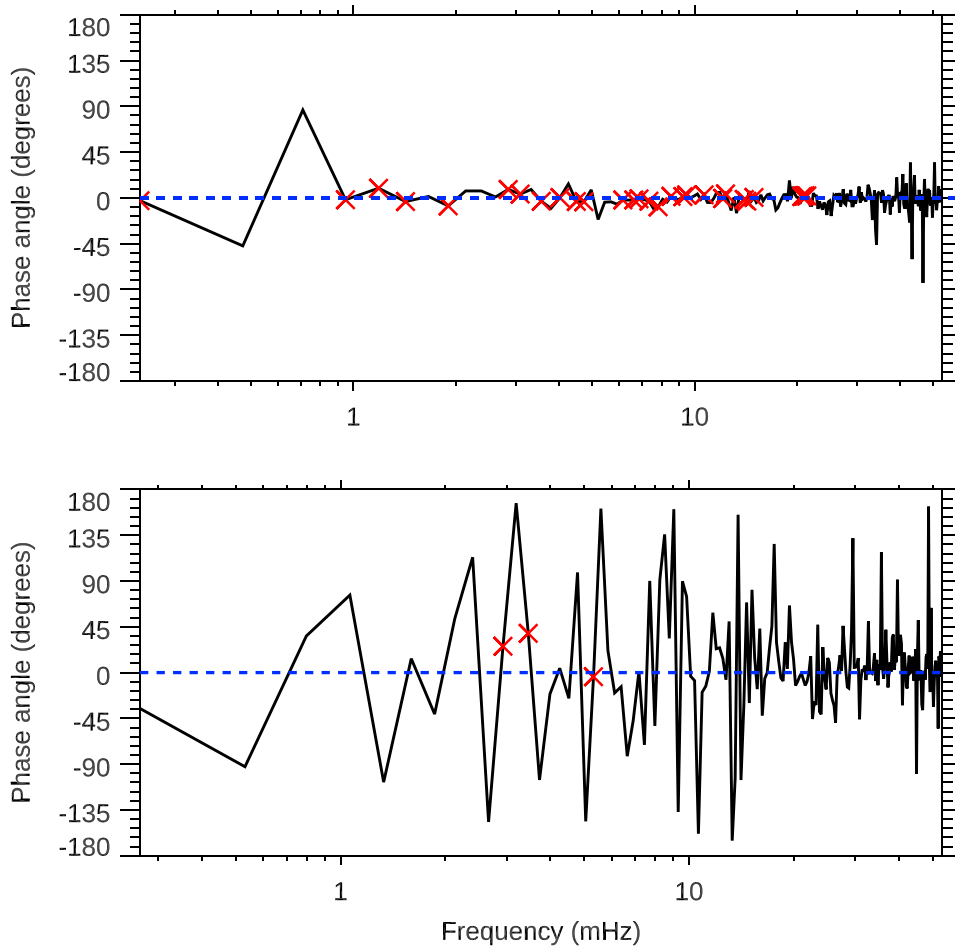
Figure 11. Both panels depict the phase differences for the average (Eulerian) intensities between pores P3 and P4 in different regions of the optical spectrum. The top panel highlights phases associated with the photospheric 4170 Å continuum channel, while the bottom panel documents the phases associated with the chromospheric line core of the Ca II 8542 Å spectral line. The red crosses indicate coherent frequencies above the 95% confidence threshold, with a blue dashed line in each panel showing the location of zero degrees, indicative of "in-phase" oscillations.

$P2 = I_{mean} - 1.60\sigma$, $P3 = I_{mean} - 2.05\sigma$, $P4 = I_{mean} - 2.20\sigma$, and $P5 = I_{mean} - 1.50\sigma$ (see the lower panel of Figure 3).

From inspection, pores P3 and P4 continue to be the largest and most complementary to each other, so a focus is placed on them. Figure 11 displays the phase relationship between the Eulerian Ca II 8542 Å line-core intensities of pores P3 and P4 (lower panel), alongside a direct comparison to the ROSA 4170 Å continuum Eulerian intensity phases of the same pores (upper panel), as established in Section 3.1. The validity of the Fourier analysis technique is confirmed by the derived photospheric phases (upper panel of Figure 11), showing the same range of in-phase behavior for frequencies $\geqslant 1$ mHz as found in the previous wavelet analyses. Most notably, however, is the large discrepancy between the behaviors of the photospheric and chromospheric phase relationships, which can be seen by comparing the upper and lower panels of Figure 11.

Of the frequencies displaying wave activity exceeding a 95% confidence threshold in the Ca II 8542 Å line core (red crosses in the lower panel of Figure 11), only the predominant 5 mHz signal exhibits any in-phase signatures between pores P3 and P4, with the other identified frequencies falling 30°–45° out of phase. Alongside this, the clearest contrast is found in the reduction in correlated chromospheric frequencies, with only three frequencies in the 3–5 mHz range, which do not necessarily represent the strongest detected power spectral

densities (see, e.g., Figure 10). This behavior is seen for the bisector Doppler velocities derived across all percentage line depths, with the sharp reduction in interpore in-phase signatures occurring around the cutoff height (~40% line depth). The extinction of lower frequencies is to be expected, as a result of the cutoff effect within this region. However, no simple process can account for the chromospheric frequencies falling out of phase with one another between neighboring pores, including powerful frequencies around 4 mHz and those close to 7 mHz (see Figure 10). The reduction in in-phase behavior cannot be a result of instrumentation, as the 9.8 s cadence of the chromospheric IBIS observations places the Nyquist frequency well above the frequency interval being discussed. Instead, the effect may be a result of pore structuring and the evolution experienced as the waveguides extend through the stratified atmosphere.

Next, the phase relationships between the Ca II 8542 Å line-core intensities, I, and the derived line-core Doppler velocities, v_{LOS}, were studied for each pixel contained within the pores. The aggregated result for the I–V phases within each pixel of pore P3 is displayed in Figure 12, which is representative of the general trend across all chromospheric pore measurements captured in our observing sequence. From inspection of Figure 12, the I–V measurements are consistently out of phase, with average phase lags of ~40°–70° across all frequencies.
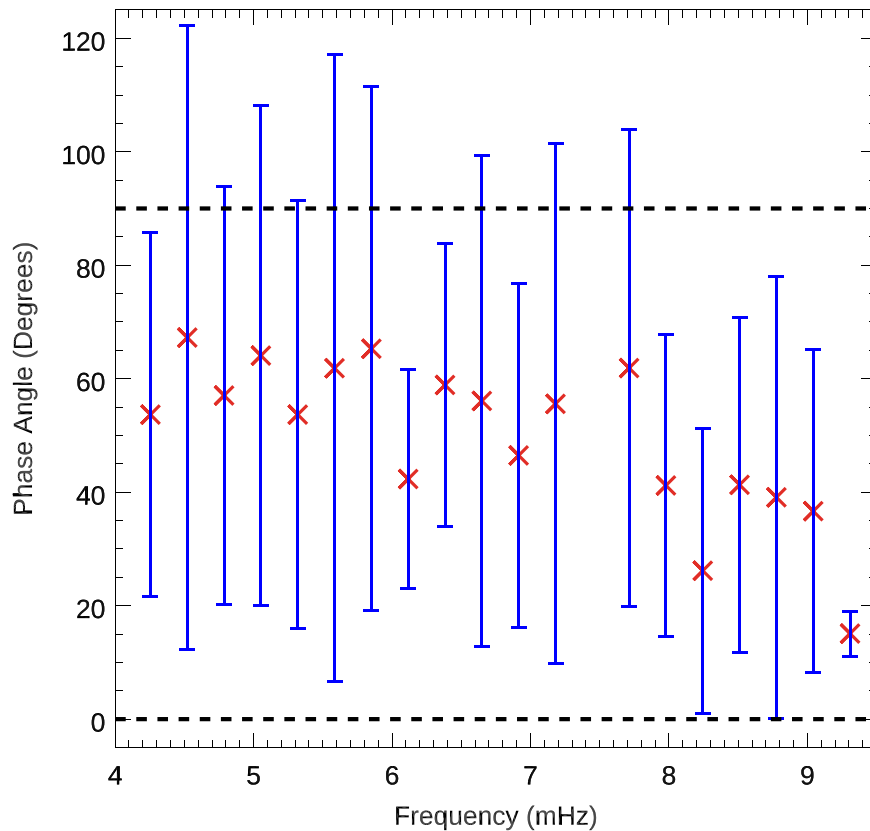
Figure 12. Average phase differences (red crosses) between oscillations in the Ca II 8542 Å line-of-sight velocity, v_{LOS}, and associated line-core intensities of the pixels contained within pore P3. The error bars (blue) represent the standard deviation of the measured I–V phases at each frequency, with horizontal dashed black lines highlighting the 0° and 90° phase angles for reference.

Furthermore, each frequency displays a significant spread of phases across the body of the pore, with standard deviations on the order of the mean phase value. Natural variance in I–V is expected at chromospheric heights due to aspects of radiative damping (Severino et al. 2013), but not to the extent observed in Figure 12 indicative of a nonunified structuring of wave activity. In larger flux tubes, such as sunspots, certain wave modes have been observed to oscillate in a monolithic fashion radially across the tube, akin to a drum skin (Jess et al. 2012a; Stangalini et al. 2021, 2022). However, recent work has revealed that on small scales, sunspots show a "corrugated" magnetic structure, with a range of fibrils permeating across the flux tube (Rouppe van der Voort & de la Cruz Rodríguez 2013; Yurchyshyn et al. 2014; Nelson et al. 2017). It was shown that these fields cause phase shifts in nonlinear magnetoacoustic shocks in the umbra (Henriques et al. 2020). In the case of the pores presented in the current study, no subregions exhibit spatial coherence, suggesting that the pores manifest as a collection of fractured waveguides in the chromosphere, rather than as a single monolithic tube as in the photosphere. This is consistent with the corrugated model of Henriques et al. (2020), where the corrugation leads to the annihilation of in-phase interpore frequencies, as the oscillations within each pore propagate in their own unique manner that is governed by magnetic field inclination changes across the pore and the small-scale plasma flows associated with a corrugated atmosphere. Hence, despite the wave power existing across all flux tubes, they no longer share the commonality they possessed upon emergence at photospheric heights.

3.2.3. Wave Propagation

GM21 reported notable energy damping of oscillations in photospheric v_{LOS} signatures in all pores as they passed through the lower atmosphere, up to an atmospheric height of approximately 500 km. The elimination of interpore coherency discussed in Section 3.2.2 does not preclude the propagation of the detected wave power within each pore, so it is pertinent to study the continuing viability of these waves as energy conduits.

The phase lags between the line-core Ca II 8542 Å intensity and its associated line-of-sight Doppler velocity, v_{LOS}, as discussed in Section 3.2.2, has previously been used to determine the precise mode of compressible sausage waves (e.g., Tsap et al. 2016). Through the derived relationships presented by Moreels & Van Doorsselaere (2013), the slow, propagating sausage mode observed by GM21 would produce an in-phase I–V relationship, i.e., a 0° phase lag, which from inspection of Figure 12 is not necessarily the case at chromospheric heights. Moreels & Van Doorsselaere (2013) allows for phase solutions in the range of 0°–90°; however, the lack of consensus on a single phase angle for each frequency (see Figure 12) suggests that the exact mode of propagation in the chromosphere is not discernible through the I–V phase alone. It must be noted that Moreels & Van Doorsselaere (2013) based their model on a photospheric flux tube; therefore, it is not unexpected that the derived relationships for compressible modes do not hold in the more complex chromosphere. Instead, bisector Doppler velocities derived from consecutively increasing percentage line depths must be employed directly to search for signatures of propagation.
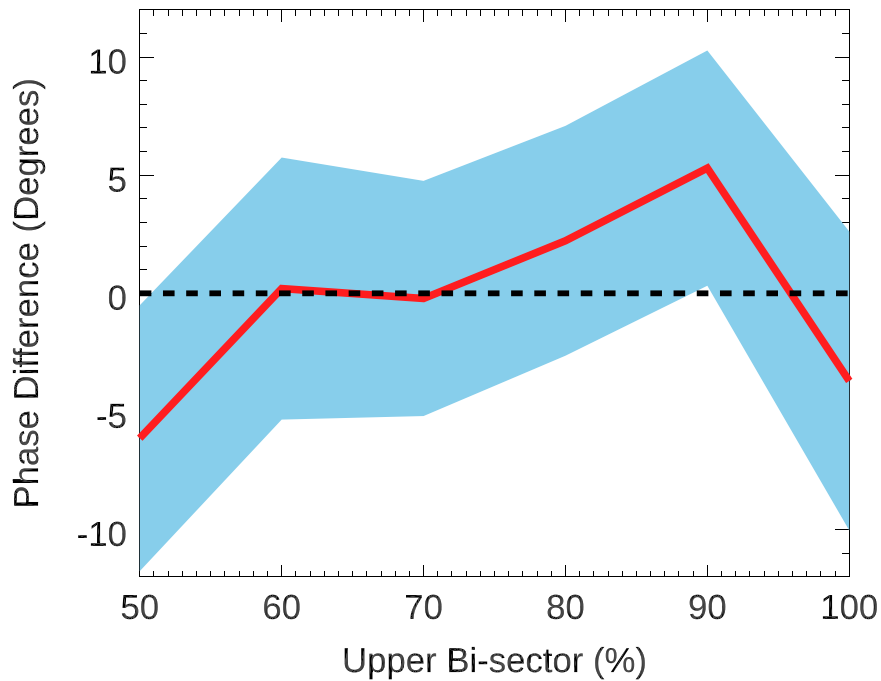
Figure 13. Phase differences for frequencies detected in the displayed bisector and the 10% lower line depth, where a negative phase angle indicates the wave is detected at the lower line depth first. The average phase difference is plotted in red, with the standard deviation of each height differential shown in blue.

To directly assess the propagation of wave signatures in the lower chromosphere of the pores, the Eulerian bisector velocities for each pore at neighboring percentage line depths were analyzed. Due to the persistence and size of pores P3 and P4, we limited our study to these long-lived and stable magnetic features. Furthermore, for consistency to previous analyses, we only select those frequencies that exceed the 95% confidence threshold across all percentage line-depth comparisons, i.e., 40%–50%, 50%–60%, 60%–70%, 70%–80%, 80%–90%, and 90%–100% (where the 100% line depth corresponds to the Ca II 8542 Å line core). In total, 11 frequencies between 4 and 6 mHz were identified in pores P3 and P4.

For the detection of definitely upwardly propagating waves, the derived phase angles would need to display clear negative phase angles (i.e., the 50% line-depth wave signals should trail their 40% line-depth counterparts). As can be seen in Figure 13, the measured phase angles between neighboring Ca II 8542 Å percentage line depths do not show clear negative phase lags, with the mean values at each line-depth interval distributed around zero degrees. Indeed, including the standard errors, each line-depth interval straddles the zero degree phase threshold, suggesting the presence of standing mode waves in the pores at chromospheric heights. Standing compressible modes have previously been observed in chromospheric magnetic flux tubes, with Freij et al. (2016) postulating that the reflection occurs at the transition region boundary, and could be indicative of a chromospheric resonator (Felipe et al. 2020; Jess et al. 2020; Felipe 2021; Jess et al. 2021). The viability of this reflection region can be assessed through calculating the typical wavelength of these standing modes. The average tube speed of the pores in the high photosphere, as inferred by GM21, of $\sim 8\,\mathrm{km\,s^{-1}}$ can be combined with the predominant 5 mHz frequency through $\lambda = v_T/f$ to give an approximate wavelength of 1600 km. This places a further node at ~ 2400 km, and considering the increase in the tube speed associated with the chromosphere leading to an increased

wavelength, there is ample opportunity for a standing mode reflection to form at transition region heights.

4. Conclusion

The nature of wave generation and chromospheric propagation within a unique cluster of five magnetic pores is presented by employing wavelet and Fourier analysis to a novel configuration of high-resolution, multiwavelength observations. This study has revealed much about the characteristics of pores as waveguides, alongside providing new mechanisms for multiheight chromospheric diagnostics. In particular:

1. Coherent oscillations in the intensity emission and cross-sectional area, consistent with slow sausage modes, were detected across all pores in the photosphere, with robust analysis concluding that instrumental noise or any mitigation techniques applied do not facilitate such coherence. The remarkable coherence across the pores is indicative of a common driver, acting on the flux tubes below the solar surface where it is believed they constitute a monolithic flux rope.

2. Ca II 8542 Å bisector analysis was employed to extract Doppler velocity signals across a range of percentage line depths and to test their viability to probe discrete heights in the lower solar atmosphere. It was found that the bisector velocities probe an atmospheric height above the cutoff region that prohibits the propagation of 3 mHz signals, and that each increasing percentage line depth exhibits a clear wave power transition toward dominant 5 mHz power, which has only been seen with such fidelity in simulations (e.g., Felipe 2019). The increasing 5 mHz wave power found as a function of the percentage line depth is indicative of the bisector velocities sampling progressively higher atmospheric heights, which was confirmed through response function calculations of the Ca II 8542 Å line.

3. The extinction of the ample photospheric wave coherency across a range of frequencies in the chromosphere was seen in Ca II 8542 Å line-core intensities and bisector Doppler velocities, with only the 5 mHz p-mode peak retaining any semblance of correlation. Phase relationships between intensity and Doppler velocity revealed the fractured nature of intrapore oscillations, with a lack of uniformity in wave phases indicative of unique propagation parameters across the surface of a single pore structure, consistent with the first detection of a corrugated atmosphere in the chromosphere of a magnetic pore.

4. The waves displayed propagation characteristics consistent with standing modes through Fourier analysis of bisector velocities derived from adjacent Ca II 8542 Å percentage line depths spanning from the photospheric wings of the profile to the chromospheric line core. Eleven frequencies, each displaying $\geqslant 95\%$ confidence levels, spanned all percentage line depths in pores P3 and P4, with phase angles between neighboring percentage line depths around zero degrees across all frequencies, indicative of standing modes formed due to a reflection layer at the base of the transition region.

The distinctive arrangement of this active region has allowed for an unprecedented study into the effects of pore structuring on wave transportation into the chromosphere, given the injection of equivalent, coherent waves at the solar surface. We have shown that the fine-scale differences in each magnetic flux tube can cause notable variations in the evolution of waves contained within. The phase differences seen in Figure 13 indicate the corrugation of the chromospheric pore atmosphere, consistent with the observations and models of Henriques et al. (2020). In their case, the larger density gradients of sunspots produced macroscopic shock events capable of highlighting the corrugation due to horizontal fibrils. As discussed in Section 3.2.1, there are no observable shock events within the pores; however this does not prohibit the existence of the small-scale brightenings associated with umbral corrugation as the filling factor of their associated pixel may be dominated by quiescent plasma. Indeed, Rouppe van der Voort & de la Cruz Rodríguez (2013) confirmed the fibrilar nature of umbrae using smaller sunspots with partial penumbra, indicating that the effect can be scaled down to smaller structures. Rather than relying on macroscopic shocks, the lack of phase across each pore provides the first evidence of corrugation in small-scale magnetic structures. Magnetic field corrugation across a range of magnetic structures would have implications on the energy transport and deposition through wave motion. However, semi-empirical modeling through inversions, similar to the robust methods of Henriques et al. (2020), would be advantageous in the future to fully assess the impact of corrugation on magnetic pores. This behavior could also be probed by considering the pores as coupled systems, with a photospheric input and a chromospheric output. The lack of a linear change in-phase as a function of the height implies that the pores form nonlinear systems, which can be identified and characterized with models such as NARMAX (Chen & Billings 1989). This would provide an unprecedented view of magnetic flux tubes as systems, and provide explanations for the complex phase relationships observed in these data. However, equivalent absolute measurements would be needed for the input and output of the system, such as the LOS velocity, which is not

possible for this study. Future observing runs that incorporate spectral imaging throughout the lower solar atmosphere could provide a novel investigation of pores as nonlinear systems.

Propagating waves are often thought to be necessary for the rapid damping observed by GM21. However, GM21 examined ∼3 mHz photospheric signals, which do not readily traverse the chromospheric boundary due to the atmospheric cutoff. Despite this, damping can still occur in standing modes through partial transmission of wave power at the upper reflective boundary, or geometric spreading and lateral wave leakage, as put forward by Riedl et al. (2021). Therefore, the confirmation of standing modes in chromospheric flux tubes does not preclude energy transport and damping, and as such active-region configurations such as these can have an influence on energy dissipation and chromospheric heating.

Looking forward, bisector analysis using the Ca II 8542 Å line has been shown to be a viable tool for extracting multiheight chromospheric information from a single observable in the case of these pores, though care must be taken to account for density enhancements in the line wings and/or nonlinear effects. Certainly for sunspots, bisector velocity studies would be better suited for spectral lines with less intensity responsiveness, such as Hα. For wave observers using cutting-edge suites such as DKIST, bisectors may provide an avenue for observing dynamic signals in the atmosphere without sacrificing temporal or spatial instrumental resolution. These modern observatories can also provide further insight into the variation in pore wave conduit behavior. Allied to this, modeling of multiple three-dimensional flux tubes in close proximity is in its infancy (e.g., Snow et al. 2018). However, there is scope for simulating scenarios similar to this active region to further constrain how flux tubes can differ, and whether they are a direct influence on one another across differing atmospheric heights. Allied to this, the future direction of observing campaigns can focus on more complex regions of monopolar flux tubes, to assess how unique the configuration and wave activity observed in this study truly is.

products used in this study can be provided upon request to the corresponding author.

ORCID iDs

S. D. T. Grant ⓘ https://orcid.org/0000-0001-5170-9747
D. B. Jess ⓘ https://orcid.org/0000-0002-9155-8039
M. Stangalini ⓘ https://orcid.org/0000-0002-5365-7546
S. Jafarzadeh ⓘ https://orcid.org/0000-0002-7711-5397
V. Fedun ⓘ https://orcid.org/0000-0002-0893-7346
G. Verth ⓘ https://orcid.org/0000-0002-9546-2368
P. H. Keys ⓘ https://orcid.org/0000-0001-8556-470X
S. P. Rajaguru ⓘ https://orcid.org/0000-0003-0003-4561
H. Uitenbroek ⓘ https://orcid.org/0000-0002-2554-1351
C. D. MacBride ⓘ https://orcid.org/0000-0002-9901-8723
W. Bate ⓘ https://orcid.org/0000-0001-9629-5250
C. A. Gilchrist-Millar ⓘ https://orcid.org/0000-0002-2593-4884

References

Albidah, A. B., Brevis, W., Fedun, V., et al. 2021, RSPTA, 379, 20200181
Banerjee, D., Erdélyi, R., Oliver, R., & O'Shea, E. 2007, SoPh, 246, 3
Beck, C., & Choudhary, D. P. 2020, ApJ, 891, 119
Bel, N., & Leroy, B. 1977, A&A, 55, 239
Braun, D. C., Labonte, B. J., & Duvall, T. L., Jr. 1988, ApJ, 335, 1015
Carlsson, M., & Stein, R. F. 1997, ApJ, 481, 500
Cauzzi, G., Reardon, K. P., Uitenbroek, H., et al. 2008, A&A, 480, 515
Cavallini, F. 2006, SoPh, 236, 415
Centeno, R., Collados, M., & Trujillo Bueno, J. 2006, ApJ, 640, 1153
Centeno, R., Collados, M., & Bueno, J. T. 2009, ApJ, 692, 1211
Chae, J., Park, H.-M., Ahn, K., et al. 2013, SoPh, 288, 89
Chen, F., Rempel, M., & Fan, Y. 2017, ApJ, 846, 149
Chen, S., & Billings, S. A. 1989, IJC, 49, 1013
Cheung, M. C. M., Rempel, M., Title, A. M., & Schussler, M. 2010, ApJ, 720, 233
Cho, K. S., Bong, S. C., Chae, J., et al. 2013, SoPh, 288, 23
Cho, K. S., Bong, S. C., Nakariakov, V. M., et al. 2015, ApJ, 802, 45
De Moortel, I., & Browning, P. 2015, RSPTA, 373, 20140269
Dorotovič, I., Erdélyi, R., & Karlovský, V. 2008, in Waves & Oscillations in the Solar Atmosphere: Heating and Magneto-Seismology, ed. R. Erdélyi & C. A. Mendoza-Briceno, Vol. 247 (Cambridge: Cambridge Univ. Press), 351, doi:10.1017/S174392130801507X
Edwin, P. M., & Roberts, B. 1983, SoPh, 88, 179
Felipe, T. 2019, A&A, 627, A169
Felipe, T. 2021, NatAs, 5, 2
Felipe, T., Kuckein, C., González Manrique, S. J., Milic, I., & Sangeetha, C. R. 2020, ApJL, 900, L29
Felipe, T., Kuckein, C., & Thaler, I. 2018, A&A, 617, A39
Felipe, T., & Sangeetha, C. R. 2020, A&A, 640, A4
Fossum, A., & Carlsson, M. 2005a, Natur, 435, 919
Fossum, A., & Carlsson, M. 2005b, ApJ, 625, 556
Freij, N., Dorotovic, I., Morton, R. J., et al. 2016, ApJ, 817, 44
(Garcia De La Rosa, J. I. 1987, SoPh, 112, 49
Gilchrist-Millar, C. A., Jess, D. B., Grant, S. D. T., et al. 2021, RSPTA, 379, 20200172
Giovanelli, R. G., Harvey, J. W., & Livingston, W. C. 1978, SoPh, 58, 347
González Manrique, S. J., Quintero Noda, C., Kuckein, C., Ruiz Cobo, B., & Carlsson, M. 2020, A&A, 634, A19
Grant, S. D. T., Jess, D. B., Moreels, M. G., et al. 2015, ApJ, 806, 132
Grant, S. D. T., Jess, D. B., Zaqarashvili, T. V., et al. 2018, NatPh, 14, 480
Henriques, V. M. J., Mathioudakis, M., Socas-Navarro, H., & Rodriguez, J. d. l. C. 2017, ApJ, 845, 102
Henriques, V. M. J., Nelson, C. J., Rouppe van der Voort, L. H. M., & Mathioudakis, M. 2020, A&A, 642, A215
Jacoutot, L., Kosovichev, A. G., Wray, A., & Mansour, N. N. 2008, ApJL, 684, L51
Jess, D. B., Andic, A., Mathioudakis, M., Bloomfield, D. S., & Keenan, F. P. 2007, A&A, 473, 943
Jess, D. B., De Moortel, I., Mathioudakis, M., et al. 2012a, ApJ, 757, 160
Jess, D. B., Shelyag, S., Mathioudakis, M., et al. 2012b, ApJ, 746, 183
Jess, D. B., Mathioudakis, M., Christian, D. J., Crockett, P. J., & Keenan, F. P. 2010a, ApJL, 719, L134
Jess, D. B., Mathioudakis, M., Christian, D. J., et al. 2010b, SoPh, 261, 363
Jess, D. B., Mathioudakis, M., & Keys, P. H. 2014, ApJ, 795, 172
Jess, D. B., Morton, R. J., Verth, G., et al. 2015, SSRv, 190, 103
Jess, D. B., Snow, B., Fleck, B., Stangalini, M., & Jafarzadeh, S. 2021, NatAs, 5, 5
Jess, D. B., Reznikova, V. E., Ryans, R. S. I., et al. 2016, NatPh, 12, 179
Jess, D. B., Doorsselaere, T. V., Verth, G., et al. 2017, ApJ, 842, 59
Jess, D. B., Dillon, C. J., Kirk, M. S., et al. 2019, ApJ, 871, 133
Jess, D. B., Snow, B., Houston, S. J., et al. 2020, NatAs, 4, 220
Kato, Y., Steiner, O., Steffen, M., & Suematsu, Y. 2011, ApJL, 730, L24
Keys, P. H., Mathioudakis, M., Jess, D. B., Mackay, D. H., & Keenan, F. P. 2014, A&A, 566, A99
Keys, P. H., Morton, R. J., Jess, D. B., et al. 2018, ApJ, 857, 28
Khomenko, E., & Collados, M. 2015, LRSP, 12, 6
Kitiashvili, I. N., Kosovichev, A. G., Mansour, N. N., & Wray, A. A. 2011, SoPh, 268, 283
Krishna Prasad, S., Jess, D. B., & Khomenko, E. 2015, ApJL, 812, L15
Kulander, J. L., & Jefferies, J. T. 1966, ApJ, 146, 194
Leenaarts, J., de la Cruz Rodriguez, J., Kochukhov, O., & Carlsson, M. 2014, ApJL, 784, L17
Leighton, R. B., Noyes, R. W., & Simon, G. W. 1962, ApJ, 135, 474
Lites, B. W. 1984, ApJ, 277, 874
Lites, B. W., White, O. R., & Packman, D. 1982, ApJ, 253, 386
MacBride, C. D., & Jess, D. B. 2020, MCALF: Multi-Component Atmospheric Line Fitting, v0.1, Zenodo, doi:10.5281/zenodo.3924527
MacBride, C., & Jess, D. 2021, JOSS, 6, 3265
MacBride, C. D., Jess, D. B., Grant, S. D. T., et al. 2021, RSPTA, 379, 20200171
Maltby, P., Avrett, E. H., Carlsson, M., et al. 1986, ApJ, 306, 284
Marino, J., Rimmele, T., & Christou, J. 2006, Proc. SPIE, 6272, 62723W
Monson, A. J., Mathioudakis, M., Reid, A., Milligan, R., & Kuridze, D. 2021, ApJ, 915, 16
Moreels, M. G., Goossens, M., & Van Doorsselaere, T. 2013, A&A, 555, A75
Moreels, M. G., & Van Doorsselaere, T. 2013, A&A, 551, A137
Moreels, M. G., Van Doorsselaere, T., Grant, S. D. T., Jess, D. B., & Goossens, M. 2015, A&A, 578, A60
Morton, R. J., Erdelyi, R., Jess, D. B., & Mathioudakis, M. 2011, ApJL, 729, L18
Narain, U., & Ulmschneider, P. 1996, SSRv, 75, 453
Nelson, C. J., Henriques, V. M. J., Mathioudakis, M., & Keenan, F. P. 2017, A&A, 605, A14
Nordlund, Å., & Stein, R. F. 2001, ApJ, 546, 576
Nordlund, Å., Stein, R. F., & Asplund, M. 2009, SoPh, 6, 2
Noyes, R. W., & Leighton, R. B. 1963, ApJ, 138, 631
Parnell, C. E., & De Moortel, I. 2012, RSPTA, 370, 3217
Priest, E. R., Chitta, L. P., & Syntelis, P. 2018, ApJL, 862, L24
Rajaguru, S. P., Sangeetha, C. R., & Tripathi, D. 2019, ApJ, 871, 155
Rast, M. P., Bello Gonzalez, N., Bellot Rubio, L., et al. 2021, SoPh, 296, 70
Riedl, J. M., Gilchrist-Millar, C. A., Van Doorsselaere, T., Jess, D. B., & Grant, S. D. T. 2021, A&A, 648, A77
Rimmele, T. R. 2004, Proc. SPIE, 5490, 34
Rimmele, T. R., Warner, M., Keil, S. L., et al. 2020, SoPh, 295, 172
Rouppe van der Voort, L., & de la Cruz Rodríguez, J. 2013, ApJ, 776, 56
Ruiz Cobo, B., & del Toro Iniesta, J. C. 1992, ApJ, 398, 375
Schmitz, F., & Fleck, B. 1998, A&A, 337, 487
Schwarzschild, M. 1948, ApJ, 107, 1
Severino, G., Straus, T., Oliviero, M., Steffen, M., & Fleck, B. 2013, SoPh, 284, 297
Snow, B., Fedun, V., Gent, F. A., Verth, G., & Erdelyi, R. 2018, ApJ, 857, 125
Sobotka, M. 2003, AN, 324, 369
Socas-Navarro, H. 2005, ApJL, 633, L57
Socas-Navarro, H., Bueno, J. T., & Ruiz Cobo, B. 2000, Sci, 288, 1396
Solanki, S. K., Riethmuller, T. L., Barthol, P., et al. 2017, ApJS, 229, 2
Srivastava, A. K., Ballester, J. L., Cally, P. S., et al. 2021, JGRA, 126, e29097
Stangalini, M., Del Moro, D., Berrilli, F., & Jefferies, S. M. 2011, A&A, 534, A65
Stangalini, M., Giannattasio, F., Del Moro, D., & Berrilli, F. 2012, A&A, 539, L4
Stangalini, M., Jess, F., Verth, D., et al. 2021, A&A, 649, A169
Stangalini, M., Verth, G., Fedun, V., et al. 2022, NatCo, 13, 479
Stein, R. F., & Nordlund, Å. 2001, ApJ, 546, 585
Steiner, O., Grossmann-Doerth, U., Knolker, M., & Schussler, M. 1998, ApJ, 495, 468
Stull, R. B. 1988, Atmospheric and Oceanographic Sciences Library, Vol. 13, An Introduction to Boundary Layer Meteorology (Dordrecht: Springer)
Torrence, C., & Compo, G. P. 1998, BAMS, 79, 61

Torrence, C., & Webster, P. J. 1999, JCli, 12, 2679
Tsap, Y. T., Stepanov, A. V., & Kopylova, Y. G. 2016, SoPh, 291, 3349
Uitenbroek, H. 2006, ApJ, 639, 516
Van Doorsselaere, T., Srivastava, A. K., Antolin, P., et al. 2020, SSRv, 216, 140
Vernazza, J. E., Avrett, E. H., & Loeser, R. 1981, ApJS, 45, 635
Verth, G., & Jess, D. B. 2016, GMS, 216, 431
Wilson, P. R., & Cannon, C. J. 1968, SoPh, 4, 3

Wiśniewska, A., Musielak, Z. E., Staiger, J., & Roth, M. 2016, ApJL, 819, L23
Withbroe, G. L., & Noyes, R. W. 1977, ARA&A, 15, 363
Wöger, F., von der Luhe, O., & Reardon, K. 2008, A&A, 488, 375
Yuan, D., Nakariakov, V. M., Huang, Z., et al. 2014, ApJ, 792, 41
Yurchyshyn, V., Abramenko, V., Kosovichev, A., & Goode, P. 2014, ApJ, 787, 58
Zwaan, C. 1985, SoPh, 100, 397